

## Research on Three-Dimensional Imaging Method Using Tensor for Electrical Impedance Tomography (EIT)

Qi Wang<sup>1, 2, 3</sup>, Lei Yu<sup>1, 2</sup>, Xiuyan Li<sup>1, 2</sup>, Xiaojie Duan<sup>1, 2</sup>, Xiaojie Li<sup>3</sup>, Huimei Ma<sup>1, 2</sup>, Jixuan Lu<sup>1, 2</sup>, Jianming Wang<sup>1, 2, \*</sup>, and Huaxiang Wang<sup>4</sup>

**Abstract**—Electrical impedance tomography (EIT) is a technique for reconstructing the conductivity distribution by injecting currents at the boundary of a subject and measuring the resulting changes in voltage. Many algorithms have been proposed for two-dimensional EIT reconstruction. However, since the human thorax has the characteristic of three-dimensions, EIT is a truly three-dimensional imaging problem. In this paper, we propose a three-dimensional imaging method using tensors for EIT. A tensor EIT model is established by EIT data, and the tucker decomposition is used to obtain the tensor basis. The tensor basis can form a new way to reconstruct image in three-dimensional space. Experiment results reveal that the data structural information of image can be fully used by the tensor method. A comparison of the peak signal to noise ratio (PSNR) shows that the newly proposed method performs better than other methods, i.e., the Dynamic Group Sparse TV algorithm and Tikhonov algorithm. The newly proposed method is closer to the ground truth, thus it can more accurately reflect the state of a lung than two-dimensional EIT. Finally, the EIT experiment is carried out to evaluate the proposed method. The experimental results show that the accuracy of reconstruction based on the new method is efficiently improved.

### 1. INTRODUCTION

Electrical impedance tomography (EIT) is an emerging imaging technology that has been developed in recent years. EIT technology is a noninvasive method to obtain the impedance information distribution within the measured object field by applying excitation current to detect the variation of the boundary voltage information of the measured object field. In recent decades, EIT technology [1] has been developed rapidly in the field of biomedical imaging, owing to its non-radiation, high-speed, and non-intrusive sensing ability. It can reconstruct the internal impedance by simultaneously measuring the voltage or current at the boundary. EIT is an attractive medical imaging technology with potential clinical application. However, maintaining high resolution in space together with low costs is still challenging.

In order to meet the requirement of mathematical model and reduce the computation complexity, EIT imaging data are always represented as a vector. However, the essence of EIT data is multi-dimensional, which is similar to traditional medical imaging, such as CT and MRI [2]. According to the EIT mathematical model, the reconstructed image data are represented by vectorization, while the actual reconstruction image is two-dimensional or three-dimensional signal. As a result, the information from image domain is difficult to be used for optimization of EIT reconstruction since the spatial

---

*Received 21 December 2020, Accepted 29 January 2021, Scheduled 14 February 2021*

\* Corresponding author: Jianming Wang (wjm\_tjpu@163.com).

<sup>1</sup> Tianjin Key Laboratory of Optoelectronic Detection Technology and Systems, Tiangong University, China. <sup>2</sup> School of Electronics and Information Engineering, Tiangong University, China. <sup>3</sup> School of Life Sciences, Tiangong University, Tianjin, China. <sup>4</sup> Tianjin University, Tianjin, China.

relationships of pixels are lost. Most of EIT reconstruction algorithms have been designed for two-dimensional geometries or a single cross-sectional slice of the volume. However, it can only reveal partial information of the realistic three-dimensional objects and thus limit the capability of EIT. The path of the electric currents spread all over the three-dimensional domain, so EIT is intrinsically a three-dimensional problem. As such, off-plane conductivity changes generally affect the solutions of the electrode plane and create considerable distortions in the resulting two-dimensional images. These severe limitations to two-dimensional EIT thus encourage the development of three-dimensional reconstruction.

At present, the traditional EIT image reconstruction algorithms [3, 4] include sensitivity coefficient method [5–7], iterative algorithm [8], conjugate gradient method [9], and TV regularization [10, 11]. The sensitivity coefficient method [5] is a simple image reconstruction algorithm, but the image reconstruction quality is not high because approximate substitution is used in the calculation process. LSQR algorithm [12, 13] introduces the double-diagonal matrix and QR decomposition method, which can effectively improve the computational efficiency. However, in the process of three-dimensional imaging, the amounts of measured data and reconstructed image data increase exponentially, which restricts the imaging speed. Conjugate gradient method [9] has fast convergence and small storage capability, but imaging results are susceptible to noise. TV regularization [14, 15] is a kind of regularization based on L1 norm, which can maintain a clear interface, protect image edges, and improve the accuracy of reconstructed images. However, TV regularization technique usually focuses on the global characteristics of the conductivity distribution, and constraint is posed on the image as a whole. Recently, the effect of regional structure information on image quality improvement has aroused a lot of interest. Group sparsity method [16] utilizes structure information as boundaries, which can obtain distinct boundary of inclusions. However, most of reconstruction algorithms for EIT are based on two-dimensional space. They may destroy the inherent structure of the image and fail to make full use of the information in the three-dimensional image field. Therefore, how to make full use of EIT image information on time and space scale to improve the quality of reconstruction is still challenging.

In this paper, we propose a three-dimensional imaging method using tensors for EIT. The structural information of images can be fully used by the tensor method. By means of tensors representation of image, the higher-order features of image can be preserved, and the loss of image information can be avoided. Images based on low-rank tensors are regarded as three-dimensional tensors, and their expansion matrices on time and space scales respectively represent the strong correlation of image frames on time series, and the weak correlation between pixels on space scales of a single frame, which can effectively improve the quality of image reconstruction. The reconstruction quality of the new method is compared with that of the Dynamic Group Sparse TV algorithm and the Tikhonov algorithm. Both simulated and experiment results show that EIT reconstruction based on tensors representation has better spatial resolution and noise reduction performance than traditional algorithms.

The paper is organized as follows. The second part covers the basics of EIT reconstruction. The third part explains the simulation of three-dimensional thorax contour model. In the fourth part, an EIT image reconstruction algorithm using tensors is proposed. The fifth part shows the experimental results. Finally, the sixth part gives a summary of the paper.

## 2. PRINCIPLE OF EIT IMAGE RECONSTRUCTION

The relationship between the conductivity distribution and the measured boundary voltage is expressed as:

$$V = F(\sigma) + e \quad (1)$$

where  $F$  is the nonlinear forward operator,  $\sigma$  the conductivity variation with respect to the reference conductivity distribution in the sensing domain, and  $e$  the measurement noise. In practical scenarios, Equation (1) can be linearized and formulated as

$$V = J\sigma + e \quad (2)$$

where  $V$  is the normalized voltage measurement,  $J$  the Jacobian matrix or sensitivity matrix [17], and  $\sigma$  the conductivity variation vector between the object field and reference field. In this paper, pulmonary emptying cases are used as the reference conductivity image.

To estimate the conductivity distribution from boundary voltage measurements, an inverse problem needs to be solved. A commonly used method to solve this problem is reformulating it into a Tikhonov regularization problem

$$\arg \min_{\sigma} \left\{ \|J\sigma - V\|_2^2 + \lambda \|\sigma\|_2^2 \right\} \quad (3)$$

where  $\lambda$  is the super-parameter. The Tikhonov regularization is an L2-norm-based regularization and is best suited for a smooth model  $\sigma$ . EIT inversion with the Tikhonov regularization produces blurred interfaces for piecewise-constant conductivity models. To help preserve sharp interfaces in subsurface structures, TV regularization is incorporated into the EIT model, leading to

$$\arg \min_{\sigma} \left\{ \|J\sigma - V\|_2^2 + \lambda \|\sigma\|_{TV} \right\} \quad (4)$$

where the TV-norm for a 3D model is defined as

$$\begin{aligned} \|\sigma\|_{TV} &= \sum_{i,j,k} \sqrt{|\nabla_x \sigma|_{i,j,k}|^2 + |\nabla_y \sigma|_{i,j,k}|^2 + |\nabla_z \sigma|_{i,j,k}|^2} \\ (\nabla_x \sigma)_{i,j,k} &= \sigma_{i+1,j,k} - \sigma_{i,j,k} \\ (\nabla_y \sigma)_{i,j,k} &= \sigma_{i,j+1,k} - \sigma_{i,j,k} \\ (\nabla_z \sigma)_{i,j,k} &= \sigma_{i,j,k+1} - \sigma_{i,j,k} \end{aligned} \quad (5)$$

where  $(\nabla_x \sigma)$ ,  $(\nabla_y \sigma)$  and  $(\nabla_z \sigma)$  are the first-order local differences of the three-dimensional model in the  $x$ ,  $y$ , and  $z$  dimensions, respectively. The indexes  $i$ ,  $j$ , and  $k$  refer to elements in the finite element mesh. In traditional TV solution, a smoothing parameter  $\epsilon$  is always introduced to approximate the original TV term to make it differentiable at the origin:

$$\|\sigma\|_{TV,\epsilon} = \sum_{i,j,k} \sqrt{|\nabla_x \sigma|_{i,j,k}|^2 + |\nabla_y \sigma|_{i,j,k}|^2 + |\nabla_z \sigma|_{i,j,k}|^2 + \epsilon} \quad (6)$$

In order to improve the anti-noise performance, a filter is applied to Equation (6).

$$\begin{cases} |\sigma|_{i,j,k} = |\sigma|_{i,j,k}, & |\sigma|_{i,j,k} > |\sigma|_{mean} + |\sigma|_{std} \\ |\sigma|_{i,j,k} = 0, & |\sigma|_{i,j,k} \leq |\sigma|_{mean} + |\sigma|_{std} \end{cases} \quad (7)$$

where  $|\Delta\sigma|_{mean}$  is the mean of  $\Delta\sigma$  absolute value, and  $|\Delta\sigma|_{std}$  is the variance of  $\Delta\sigma$  absolute value.

### 3. SIMULATION OF THREE-DIMENSIONAL CHEST CONTOUR MODEL

To obtain 3D reconstruction results, the image could be reconstructed onto multiple voxel layers perpendicular to the  $z$ -axis with the measurements from multi-ring electrode planes. Considering the memory limits and speed requirements, there are 111 reconstruction layers for 3D reconstructed image, i.e., the reconstruction layer separation is 0.25 cm. A three-dimensional mesh for the inverse problem is developed as shown in Fig. 1, where the illustrated sensing domain is longitudinally divided into 111 layers, and each layer has the resolution of  $32 \times 32$ .

By calculating and plotting the imaging relative error between the reconstructed images and the real conductivity distribution on each layer, we selected 20 reconstructed layers, i.e., 5 cm between adjacent rings for measurement. As a result, 5 electrode rings with 16 electrodes on each ring are used to cover the measurement of the whole thorax area. The models with 5 electric rings are shown in Fig. 2. This leads to the improved spatial resolution on the  $z$ -axis and reduces the influence of off-plane objects [18].

### 4. TENSOR BASED EIT IMAGE RECONSTRUCTION

This section briefly introduces some basic tensors used in this paper and proposes a 3D electrical impedance imaging algorithm using tensors. The simulation experiment is conducted through the 3D thoracic contour model established in the second section to verify the reconstruction image quality of this algorithm.

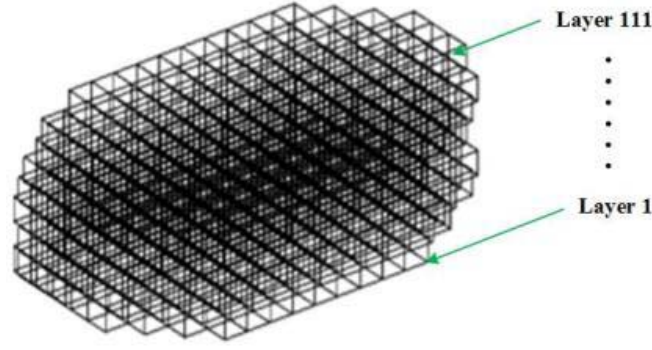


**Figure 1.** Voxel mesh for inverse problem calculation.

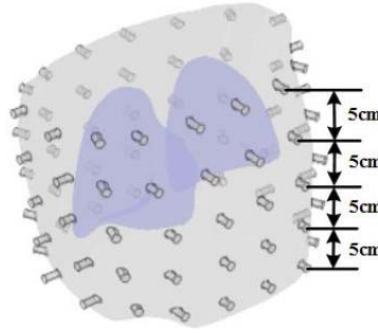


**Figure 2.** 3D thorax models with designed 5 electric rings.

#### 4.1. Basic Knowledge of Tensors

$\underline{\mathbf{X}} \in \mathbb{R}^{I_1 \times I_2 \times \dots \times I_N}$  is an  $N$ -th order tensor, and the matrix  $\mathbf{X} \in \mathbb{R}^{I_1 \times I_2}$  and the vector  $\mathbf{x} \in \mathbb{R}^I$  are special cases of tensors. The Frobenius norm is defined by  $\|\underline{\mathbf{X}}\|_F = \sqrt{\sum_{i_1 \dots i_N} x_{i_1 i_2 \dots i_N}^2}$ , where  $x_{i_1 i_2 \dots i_N}$  is an element of the tensor.

The matricization, also known as unfolding or flattening, is the process of reordering the elements of a tensor into a matrix. Mode- $n$  unfolding of a tensor  $\underline{\mathbf{X}} \in \mathbb{R}^{I_1 \times I_2 \times \dots \times I_N}$  yields a matrix  $\mathbf{X}_{(n)} \in \mathbb{R}^{I_n \times \overline{I_n}}$  ( $\overline{I_n} = \prod_{m \neq n} I_m$ ), a tensor element ( $\mathcal{X}_{i_1 i_2 \dots i_N}$ ) maps to matrix element ( $\mathbf{X}_{i,j}$ ), where  $j = 1 + \sum_{k \neq n} (i_k - 1)J_k$  with  $J_k = \prod_{m \neq n} I_m$  [19].

In order to capture the potential patterns and important features in the signal and to remove the redundant components of the original data, the Tucker decomposition is often performed on the tensor. The Tucker decomposition can be regarded as the generalization of the singular value decomposition of the matrix. Tucker decomposition [20] is the decomposition of an  $n$ -order tensor  $\underline{\mathbf{X}} \in \mathbb{R}^{I_1 \times I_2 \times \dots \times I_N}$  into an  $n$ -mode product of a core tensor  $\underline{\mathbf{G}} \in \mathbb{R}^{J_1 \times J_2 \times \dots \times J_N}$  and factor matrices  $\mathbf{A}_1, \mathbf{A}_2, \dots, \mathbf{A}_N$ , i.e.,

$$\underline{\mathbf{X}} = \underline{\mathbf{G}} \times_1 \mathbf{A}_1 \times_2 \dots \times_N \mathbf{A}_N \quad (8)$$

where  $\mathbf{A}_k \in \mathbb{R}^{I_k \times J_k}$  ( $k = 1, \dots, N$ ) are orthogonal.

Given a tensor  $\underline{\mathbf{X}} \in \mathbb{R}^{I_1 \times I_2 \times \dots \times I_N}$  and a matrix  $\Phi \in \mathbb{R}^{J \times I_n}$ , the mode- $n$  tensor is obtained by matrix product  $\underline{\mathbf{Y}} = \underline{\mathbf{X}} \times_n \Phi \in \mathbb{R}^{I_1 \times \dots \times I_{n-1} \times J \times I_{n+1} \times \dots \times I_N}$ . The element of  $\underline{\mathbf{Y}}$  is defined by:

$$\mathcal{Y}_{i_1 \dots i_{n-1} j i_{n+1} \dots i_N} = \sum_{i_n=1}^{I_n} \mathcal{X}_{i_1 \dots i_n \dots i_N} \phi_{j i_n} \quad (9)$$

with  $i_k = 1, 2, \dots, I_k$  ( $k \neq n$ ) and  $j = 1, 2, \dots, J$ . It should be noted that this corresponds to the product of matrix  $\Phi$  by each one of the mode- $n$  fibers of  $\underline{\mathbf{X}}$  since  $\mathbf{Y}_{(n)} = \Phi \mathbf{X}_{(n)}$ .

## 5. SIMULATION EXPERIMENT

In order to make full use of the multi-dimensional property of image data, a tensor model  $\underline{\mathbf{X}} \in \mathbb{R}^{p \times q \times m}$  is constructed based on the image resolution ( $p \times q$ ) and the number of layers ( $m$ ). The boundaries of reconstructed images for EIT are related to the location of electrodes and the thorax contour of the human body, which vary with different parts of the body. As a result, the boundary shapes of reconstructed images are irregular, not only for 2D reconstruction, but also for each cross-sectional slice of the volume. In this paper, the zero-filling method [21] is extended to 3D EIT reconstruction. We consider the effective pixel number of each image ( $L$ ), the total pixel number of each reconstructed image ( $n$ ), and the number of image layers ( $m$ ). Let  $P_{Ei} \in \mathbb{R}^{L \times n}$  define effective pixel selection and  $P_{Li} \in \mathbb{R}^{n \times m}$  define image layer selection. The conductivity distribution can be represented as  $\Delta\sigma_i = P_{Ei}P_{Li}\Delta\sigma$ . Fig. 3 is the EIT pixel expansion schematic.

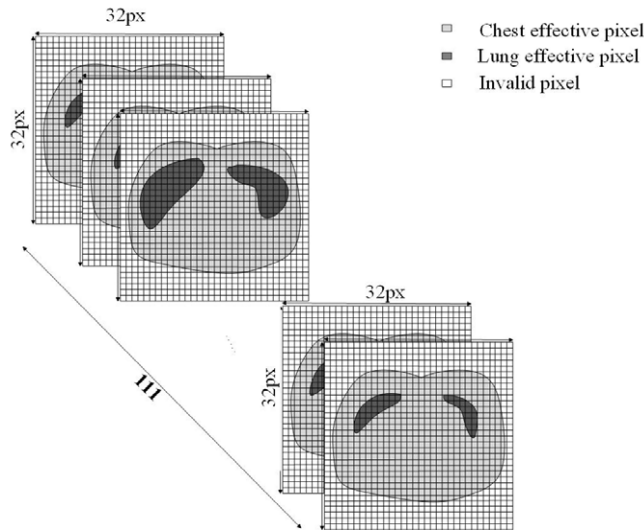


**Figure 3.** EIT pixel expansion schematic.

As discussed in Section 2, the simulation voltage can be obtained by the thorax simulation model. The change  $\Delta\sigma \in \mathbb{R}^{N \times 1}$  of conductivity can be further estimated through Equation (6). In this paper, the effective pixel of each layer image is extracted by zero-filling method. Because the resolution of each image layer is  $32 \times 32$ , changes in conductivity are extended to the matrix of size  $32 \times 32$ . The 111 layers are stacked in the  $z$  axis direction. The third order tensor  $\underline{\mathbf{X}} \in \mathbb{R}^{32 \times 32 \times 111}$  is constructed.

In practical applications, the data tensor  $\underline{\mathbf{X}}$  is not in full rank, but has a good low linear-rank approximation. Therefore, an image signal can be written as [22]:

$$\underline{\mathbf{X}} = \underline{\mathbf{X}}_0 + \underline{\mathbf{E}} \quad (10)$$

where  $\underline{\mathbf{X}}_0$  is a multilinear-rank-(32,32,111) tensor approximation, and  $\underline{\mathbf{E}}$  is an error tensor.

The tensor  $\underline{\mathbf{X}}$  can obtain low linear-rank tensor  $\underline{\mathbf{X}}_0$  by Tucker higher-order orthogonal iteration, which is defined as follows:

$$\underline{\mathbf{X}}_0 = \underline{\mathbf{G}} \times_1 \mathbf{A}_1 \times_2 \mathbf{A}_2 \times_3 \mathbf{A}_3 \quad (11)$$

$$\mathbf{A}_n = \mathbf{U}_n (\Phi_n \mathbf{U}_n)^{-1} \quad (12)$$

with a core tensor  $\underline{\mathbf{G}} \in \mathbb{R}^{32 \times 32 \times 111}$  and factor matrices  $\mathbf{A}_1 \in \mathbb{R}^{32 \times 32}$ ,  $\mathbf{A}_2 \in \mathbb{R}^{32 \times 32}$ ,  $\mathbf{A}_3 \in \mathbb{R}^{111 \times 111}$ , HOSVD [20] factorized orthogonal matrix  $\mathbf{U}_n$ , as shown in Fig. 4.

According to the definition of the mode- $n$  product in Eq. (8), we use multidimensional structure of tensors to obtain the compression measurement sets. Therefore, the compressed multichannel

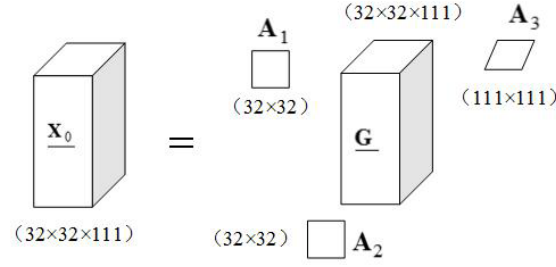


**Figure 4.** Tucker decomposition diagram of the 3rd-order tensor.

measurement set  $\underline{\mathbf{Z}}^{(n)}$  ( $n = 1, 2, 3$ ) is calculated by the following formula:

$$\begin{aligned}\underline{\mathbf{Z}}^{(1)} &= \underline{\mathbf{X}} \times_2 \Phi_2 \times_3 \Phi_3 \\ \underline{\mathbf{Z}}^{(2)} &= \underline{\mathbf{X}} \times_1 \Phi_1 \times_3 \Phi_3 \\ \underline{\mathbf{Z}}^{(3)} &= \underline{\mathbf{X}} \times_1 \Phi_1 \times_2 \Phi_2\end{aligned}\quad (13)$$

where  $\Phi_n \in \mathbb{R}^{R_n \times I_n}$  are the mode- $n$  sensing matrices [23], which are set as identity matrices in this paper.

By the compressed multichannel measurement set  $\underline{\mathbf{Z}}^{(n)}$  ( $n = 1, 2, 3$ ), tensor  $\underline{\mathbf{W}} = \underline{\mathbf{Z}}^{(n)} \times_n \Phi_n$ ,  $\forall n$  can be obtained, as expressed in Fig. 5.

$$\underline{\mathbf{W}} = \underline{\mathbf{X}} \times_1 \Phi_1 \times_2 \Phi_2 \times_3 \Phi_3 \quad (14)$$

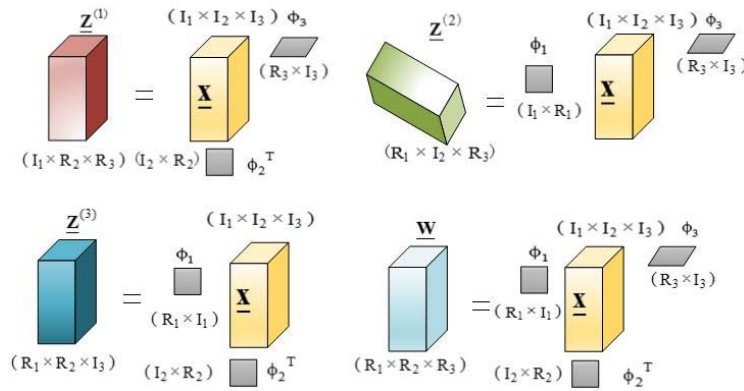


**Figure 5.** A multiplex compression measurement set of the 3rd-order tensor  $I_n R_n$  ( $n = 1, 2, 3$ ) represent the dimension of the tensor.

By combining Equations (13) and (14), the reconstruction formula can be obtained as follows:

$$\hat{\underline{\mathbf{X}}} = \underline{\mathbf{W}} \times_1 \mathbf{Z}_1 \mathbf{W}_{(1)}^+ \times_2 \mathbf{Z}_2 \mathbf{W}_{(2)}^+ \times_3 \mathbf{Z}_3 \mathbf{W}_{(3)}^+ \quad (15)$$

where “+” stands for the Moore-Penrose (MP) of a matrix, and  $\mathbf{Z}_n$  is the mode- $n$  unfolding of the compressed multiplex measure set  $\underline{\mathbf{Z}}^{(n)}$  ( $n = 1, 2, 3$ ).

As shown in Formula (16), a tensor  $\underline{\mathbf{W}} \in \mathbb{R}^{32 \times 32 \times 111}$  can be unfolded in three modes, and the unfolding diagram is shown in Fig. 6.

$$\begin{aligned}\mathbf{W}_{(1)} &= [\underline{\mathbf{W}}(:, :, 1), \underline{\mathbf{W}}(:, :, 2), \dots, \underline{\mathbf{W}}(:, :, 111)] \in \mathbb{R}^{32 \times 3552} \\ \mathbf{W}_{(2)} &= [\underline{\mathbf{W}}(:, :, 1)^T, \underline{\mathbf{W}}(:, :, 2)^T, \dots, \underline{\mathbf{W}}(:, :, 111)^T] \in \mathbb{R}^{32 \times 3552} \\ \mathbf{W}_{(3)} &= [\underline{\mathbf{W}}(:, 1, :)^T, \underline{\mathbf{W}}(:, 2, :)^T, \dots, \underline{\mathbf{W}}(:, 111, :)^T] \in \mathbb{R}^{111 \times 1024}\end{aligned}\quad (16)$$

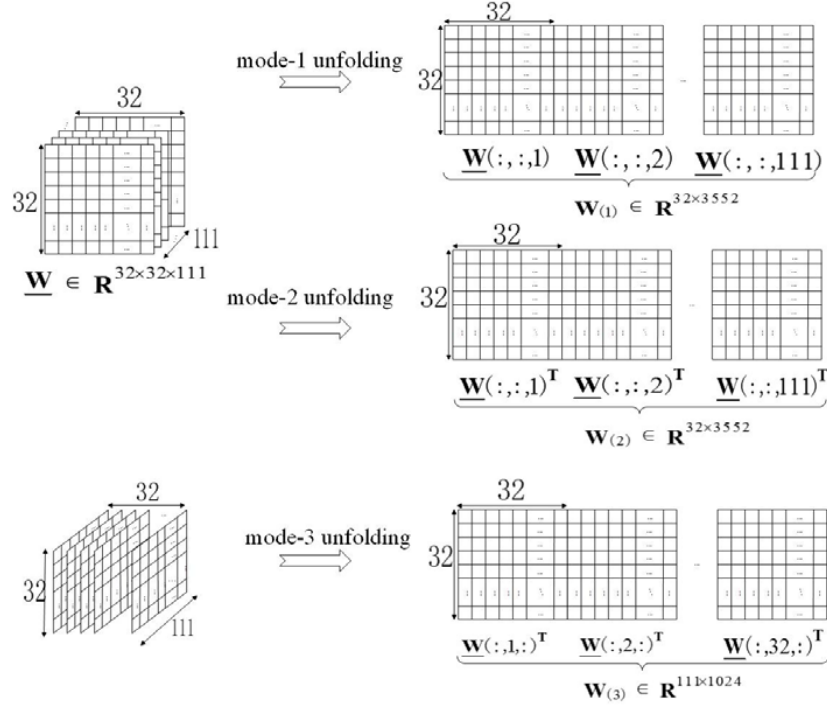


**Figure 6.** The unfolding diagram of the 3rd-order tensor  $\underline{\mathbf{W}}$ .

In particular, the reconstruction method is stable if the obtained error  $\|\underline{\mathbf{X}} - \hat{\underline{\mathbf{X}}}\|_F$  is comparable to the input error, i.e.,  $\|\underline{\mathbf{X}} - \hat{\underline{\mathbf{X}}}\|_F \sim \epsilon$ , where  $\underline{\mathbf{X}}$  is a tensor that rearranges the real pixel values, and  $\hat{\underline{\mathbf{X}}}$  is the data reconstructed by Equation (15). However, Equation (15) may suffer from an unstable behavior, which generates large output errors. So we can solve this unstable behavior by using the truncated pseudo-inverse. The truncated Moore-Penrose pseudo-inverse is defined as follows [24]:

$$\mathbf{W}^{*\tau} = \mathbf{V}\mathbf{S}^{*\tau}\mathbf{U}^T \tag{17}$$

where  $\tau$  is a threshold parameter. It is noted that  $\mathbf{W}^{*\tau} \rightarrow \mathbf{W}^+$  as  $\tau \rightarrow 0$ .

Entries of the diagonal matrix are defined as follows:

$$\sigma_i^* = \begin{cases} \frac{1}{\sigma_i}, & \sigma_i > \tau \\ 0, & \sigma_i \leq \tau \end{cases} \tag{18}$$

In other words, we define the modified reconstruction formula as follows [25]:

$$\begin{aligned} \hat{\underline{\mathbf{X}}}_\tau &= \underline{\mathbf{W}} \times_1 \mathbf{Z}_1 \mathbf{W}_{(1)}^{*\tau} \times_2 \mathbf{Z}_2 \mathbf{W}_{(2)}^{*\tau} \times_3 \mathbf{Z}_3 \mathbf{W}_{(3)}^{*\tau} \\ \mathbf{Z}_n &\equiv \left( \underline{\mathbf{Z}}^{(n)} \right)_{(n)} \quad (n = 1, 2, 3) \end{aligned} \tag{19}$$

where  $\mathbf{W}_{(n)}^{*\tau}$  is the truncated pseudo-inverse of  $\mathbf{W}_{(n)}$ , and  $\mathbf{Z}_n$  is the mode- $n$  unfolding of compressed multiplex measure sets  $\underline{\mathbf{Z}}^{(n)}$ .

Figure 7 illustrates that the original tensor  $\underline{\mathbf{X}}$  can be recovered from multi-channel measurement set  $\underline{\mathbf{Z}}^{(n)}$  and  $\underline{\mathbf{W}}$ .

By analyzing Equations (10) and (14), the error bound is defined as:

$$\begin{aligned} \|\underline{\mathbf{X}} - \hat{\underline{\mathbf{X}}}_\tau\|_F &\leq \begin{cases} b\epsilon + c\frac{\epsilon^2}{\sigma_R}, & \tau \leq \underline{\sigma} \\ a\tau + b\epsilon + c\frac{\epsilon^2}{\tau}, & \tau > \underline{\sigma} \end{cases} \\ a &= \left( \sqrt{R_1} + \sqrt{R_2} + \sqrt{I_3} \right) \|\mathbf{A}_1\| \|\mathbf{A}_2\| \end{aligned} \tag{20}$$

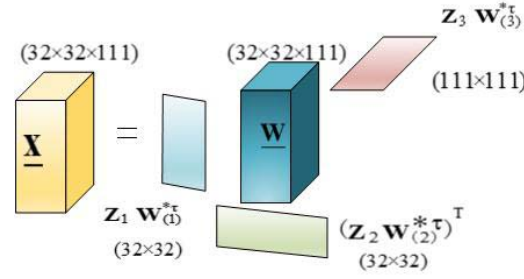


**Figure 7.** Multilinear-rank-(R1, R2, R3) restoration of 3rd-order tensor.

$$b = 1 + \|\mathbf{A}_1 \Phi_1\| \|\mathbf{A}_2 \Phi_2\| + \|\mathbf{A}_1\| (1 + \|\mathbf{A}_2 \Phi_2\|) \|\Phi_1\| + \|\mathbf{A}_2\| (1 + \|\mathbf{A}_1 \Phi_1\|) \|\Phi_2\|$$

$$c = (1 + \|\mathbf{A}_1 \Phi_1\|)(1 + \|\mathbf{A}_2 \Phi_2\|) \|\Phi_1\| \|\Phi_2\|$$

where  $\sigma_R = \sigma_{R_1} = \sigma_{R_2}$ ,  $\bar{\sigma} = \max(\sigma_R, \sigma_{R_3})$ ,  $\underline{\sigma} = \min(\sigma_R, \sigma_{R_3})$  (i.e., the maximum and minimum of the smallest singular values of the mode- $n$  unfolding matrices  $\mathbf{W}_{(n)}$ ).

The threshold  $\tau$  which determines the truncated MP pseudo inverse of  $\mathbf{W}$  and reference Equation (18) is defined as follows:

$$\tau = \epsilon \sqrt{\frac{c}{a}} \quad (21)$$

The error is determined empirically as  $\epsilon = 8.5 \times 10^{-20}$  in this paper.

---

### Three-dimensional imaging method using tensors for EIT

Input: The EIT measured voltage  $U$ , Jacobian matrix  $J$  and sensing matrices  $\Phi_1, \Phi_2, \Phi_3$

Output: Reconstruction of tensor  $\hat{\mathbf{X}}_\tau$

- 1: Set up a tensor model  $\mathbf{X}$ .
  - 2: Obtain the change of the conductivity value  $\Delta\hat{\sigma}$  in Equation (6).
  - 3: Estimate the filtered absolute conductivity change based on Equation (7).
  - 4: Through zero padding method,  $\Delta\hat{\sigma}$  is stacked in the  $z$  axis directions, expanded to the third order tensor  $\mathbf{X}$ .
  - 5: According to Equations (13) and (14), calculate the compression multidimensional measurement set  $\mathbf{Z}^{(n)}$  and the tensor  $\mathbf{W}$ .
  - 6: Calculate the threshold  $\tau$  in Equation (21).
  - 7: Compute  $\mathbf{W}_{(N)}^{*\tau}$  the truncated pseudo-inverse of  $\mathbf{W}_{(n)}$ .
  - 8: Calculate the reconstruction of tensor  $\hat{\mathbf{X}}_\tau$  in Equation (19).
- 

In order to evaluate the performance of the new algorithm and choose significant parameters, tests were conducted on simulated data. The EIT data could be obtained by the thorax simulation model based on the prior information of human body structure that was established by COMSOL. The reconstruction image algorithm was realized through MATLABR2013b. According to simulation results, 5 electrode rings with 16 electrodes on each ring were set up. Electrodes were used to cover the measurement. The condition at end-expiration was modeled by setting the conductivity of the lung tissue to  $\sigma_{\text{exp}} = 120$  mS/m. Other tissues not belonging to the lung were set to  $\sigma_{bkg} = 480$  mS/m [26, 27]. In order to simulate the typical noise levels in real measurement systems, Gaussian, zero mean random noise was added to the simulated voltages. The amplitude of the noise was 0.5% of simulated voltage [28]. A conventional adjacent current injection and voltage measurement strategy based on the complete electrode model were chosen consisting of 16 current excitation configurations and 13 corresponding voltage measurement configurations for each current excitation, i.e., the number of measured data was 208 for the reconstruction of one EIT image. All algorithmic programming and image reconstruction were done on a PC configured for 2.4 GHz GPU, 4 GB of memory, using MATLAB R2013b.

The quality of the reconstruction is quantified using peak signal to noise ratio (PNSR). The PNSR can be defined as

$$\text{PNSR (dB)} = 20 \log_{10} \left( \frac{\max(\mathbf{X})}{\|\hat{\mathbf{X}} - \mathbf{X}\|_F} \right) \tag{22}$$

where  $\mathbf{X}$  is a tensor that rearranges the actual pixel values, and  $\hat{\mathbf{X}}$  is the data reconstructed by the tensor reconstruction algorithm.

We could obtain construction data  $\hat{\mathbf{X}}_\tau$  through Equation (19) by the compressed multidimensional measurement set  $\mathbf{Z}^{(n)}$  ( $n = 1, 2, 3$ ) and the tensor  $\mathbf{W}$ .

In order to analyze the behavior of the reconstructions as a function of the threshold parameter  $\tau$ , the variation of PNSR versus threshold value is plotted in Fig. 8.

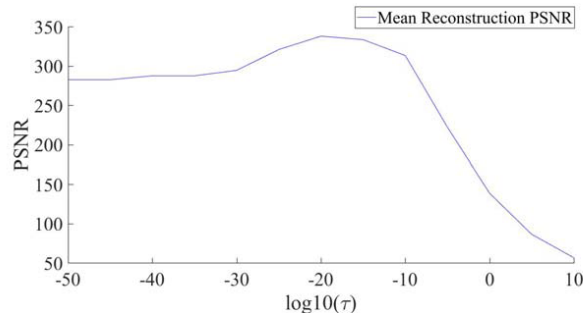


**Figure 8.** The relationship between PNSR and threshold of the tensor method.

It could be known that the PNSR of reconstructed image was the highest when  $\tau = 4.15 \times 10^{-20}$ , which means that the quality of image reconstruction was the best.

$\hat{\mathbf{X}}_\tau$  was used for three-dimensional imaging. The reconstruction results were compared with zero threshold ( $\tau = 0$ ), Dynamic Group Sparsity TV, and Tikhonov methods, as shown in Fig. 9. The results show that the nonzero threshold truncation reconstruction has higher fidelity. The tensor reconstruction algorithm makes full use of the multidimensional property of image data, so that it can retain the higher-order features of the image, avoid the loss of image information, and effectively improve the reconstruction quality of the image.

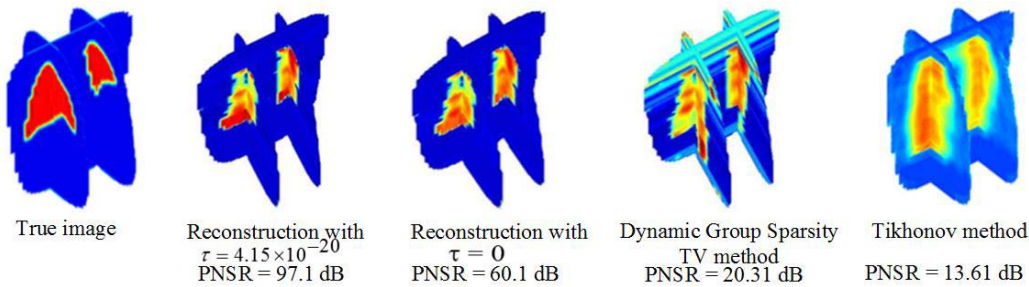


**Figure 9.** EIT 3D reconstruction results using four methods.

We selected four layers, i.e., 50th, 56th, 77th, and 87th layers which have different shapes and areas of lung in craniocaudal direction from the 111 reconstruction layers to prove the distinguish ability of 2D details in 3D EIT reconstruction results. It could be clearly found that the reconstructed image after threshold truncation can display edge information more clearly, with better imaging effect, as shown in Fig. 10.

3D reconstruction method proposed in this paper is compared with 2D reconstruction method. For 2D reconstruction, 2D current injection/voltage measurement is used for conductive distribution in each

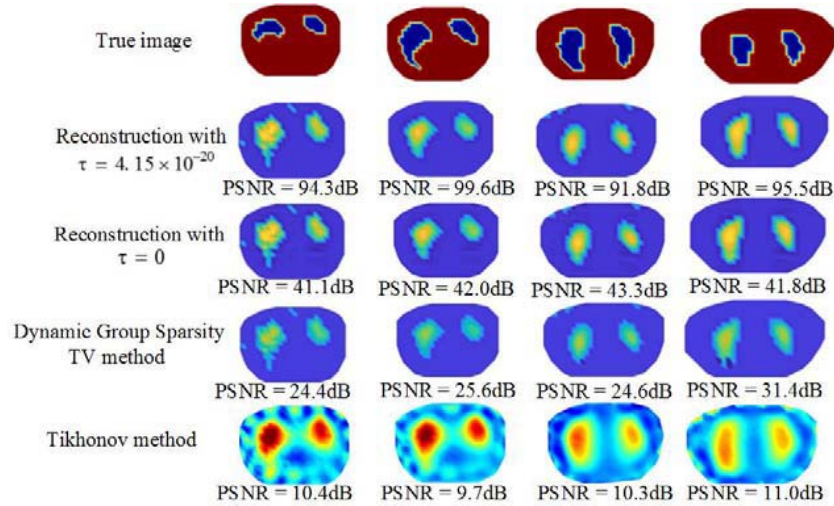


**Figure 10.** Typical 2D slices from 3D EIT reconstruction results based on four methods.

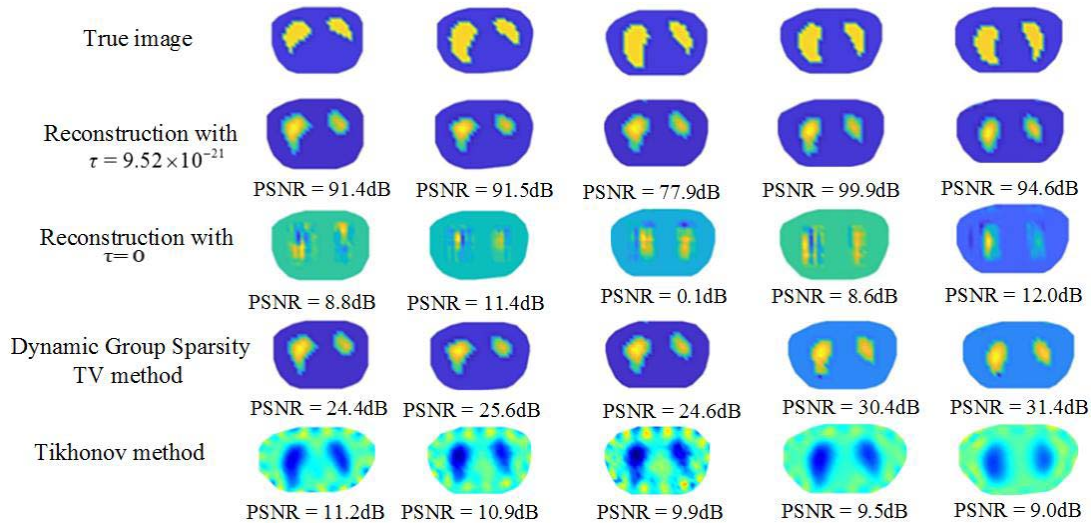


**Figure 11.** 2D EIT reconstruction results based on three methods.

slice. Because a matrix is a special form of tensor, the method is similar to the 3D tensor reconstruction method. The effective pixels are extracted and expanded to a matrix  $X$  of size  $32 \times 32$  by means of zero-fill. Formula (19) is transformed into a two-dimensional formula for EIT image reconstruction, where sensing matrices are generated randomly. Finally, the pixel value of corresponding position is selected for image display. In Fig. 11, 2D reconstruction results based on the tensor method, Dynamic Group Sparsity TV method, and Tikhonov method are compared. Obviously the imaging quality is the best when the tensor method with nonzero threshold is used. The average PSNR for all of the 111 imaging layers was calculated to be 94.39 dB.

## 6. EXPERIMENTAL RESULTS

In order to verify the feasibility of the 3D imaging method of electrical impedance using the present tensor reconstruction method, experiments were conducted with thorax phantom using a measurement setup, as shown in Fig. 12.

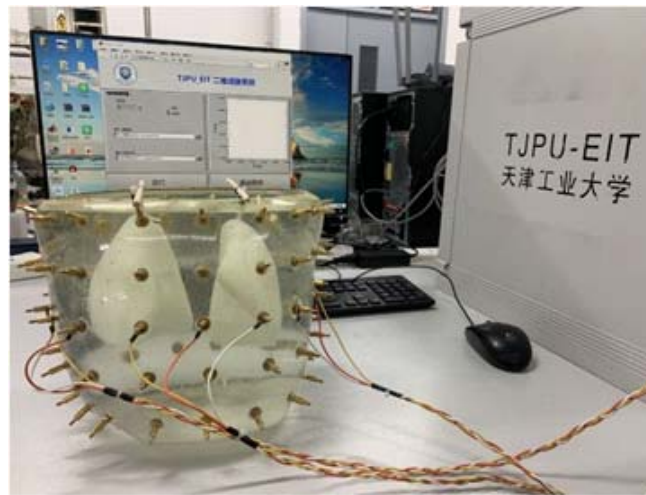


**Figure 12.** Experimental equipment for thoracic model imaging.



Clear thorax model for end-expiration

Clear thorax model for end-inspiration

(a)



Lung model for end-expiration



Lung model for end-inspiration

(b)

**Figure 13.** 3D printed phantom of thorax. (a) Thorax boundary. (b) Lungs.

We 3D printed clear thorax phantom and white lung phantom by means of a cast resin material (TN3908) according to the geometric dimension of simulation model discussed in Section 2 with 5 rings of electrodes. The 3D model of thorax boundary and lung under two respiratory conditions are shown in Fig. 13. The phantom was filled with saline solution of conductivity  $0.32 \text{ s m}^{-1}$ . The adjacent current injection and voltage measurement strategy was adopted. The amplitude of the boundary voltage measurement was used for image reconstruction. 5 mA current was injected into adjacent electrode

pairs. All measurements were made at 50 kHz.

The EIT image was reconstructed respectively by the tensor method, Dynamic Group Sparsity TV method, and Tikhonov method. The experimental imaging results are shown in Fig. 14.

In order to illustrate that the structure of lung can be fully considered by the tensor reconstruction algorithm in each layer, we selected two typical layers from the 111 layers to show the variation of lung region in craniocaudal direction, as shown in Fig. 15. The experimental results show that the proposed algorithm has superior imaging quality, compared with Dynamic Group Sparsity TV and Tikhonov method. The tensor method can more accurately reflect the state of human lung. Furthermore, since the multi-dimensional property of the image data can be fully used, the PSNR is efficiently improved.

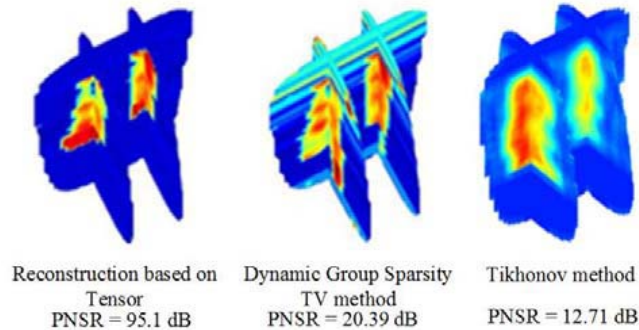


**Figure 14.** EIT 3D experimental reconstruction results using three methods.

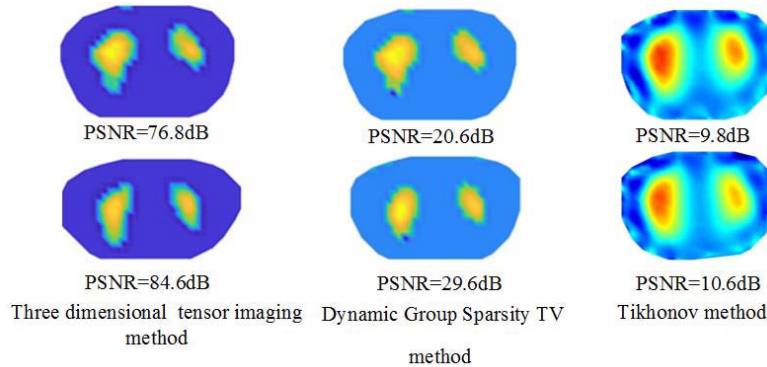


**Figure 15.** Typical 2D slices from 3D EIT experimental reconstruction results.

## 7. CONCLUSION AND FUTURE WORK

In this paper, the 3D imaging method using tensors for EIT has been successfully introduced to reconstruct EIT image. According to the vector structure of EIT data, EIT data can be expanded to tensors by the zero-filling method, then EIT images can be reconstructed using 3D imaging method. Experiment results revealed that the structural information of images could be fully used by the tensor method. The lung image is closer to the real human lung using tensors reconstruction algorithm. By comparing the PSNR of 2D and 3D reconstructed images in the above experiments, it can be found that 3D reconstruction effect is significantly better than 2D reconstruction effect. Because the ill-conditioned matrix is computed by the truncated MP pseudo-inversion, the threshold  $\tau$  is selected during EIT image reconstruction.

In future work, we will further optimize the proposed algorithm to explore a faster and better 3D imaging method with better image quality while making full use of the time and space information of the dynamic image.

## ACKNOWLEDGMENT

This research was funded by the National Natural Science Foundation of China (Grant Nos. 61872269, 61903273, 62071328 and 62072335), the Natural Science Foundation of Tianjin Municipal Science and Technology Commission (Grant No. 18JCYBJC85300), and the Tianjin Science and Technology Program (Grant No. 19PTZWHZ00020).

## REFERENCES

1. Djajaputra, D., "Electrical impedance tomography: Methods, history and applications," *Medical Physics*, Vol. 32, No. 8, 2731–2731, 2005.
2. Yu, Y., J. Jin, F. Liu, and S. Crozier, "Multidimensional compressed sensing MRI using tensor decomposition-based sparsifying transform," *PLoS ONE*, Vol. 9, No. 6, e98441, 2014.
3. Fu, H.-S. and B. Han, "Tikhonov regularization-homotopy method for electrical impedance tomography," *Journal of Natural Science of Heilongjiang University*, Vol. 3, 319–323, 2011.
4. Wang, Q., H. Wang, R. Zhang, et al., "Image reconstruction based on L1 regularization and projection methods for electrical impedance tomography," *Review of Scientific Instruments*, Vol. 83, No. 10, 104707, 2012.
5. Zhao, B., H. X. Wang, X. Y. Chen, X. L. Shi, and W. Q. Yang, "Linearized solution to electrical impedance tomography based on the Schur conjugate gradient method," *Measurement Science and Technology*, Vol. 18, No. 11, 3373–3383, 2007.
6. Morucii, J., M. Granie, M. Lei, M. Chebett, and W. Dai, "Direct sensitivity matrix in electrical impedance imaging," *International Conference of the IEEE Engineering in Medicine and Biology Society*, 538–539, 1994.
7. Barber, D. C., "A sensitivity method for electrical impedance tomography," *Clinical Physics and Physiological Measurement*, Vol. 10, No. 4, 368–371, 1989.
8. Semenov, S. Y., A. E. Bulyshev, A. E. Souvorov, et al., "Iterative algorithm for 3D EIT," *Engineering in Medicine and Biology Society*, 10, 1997.
9. Wang, M., "Inverse solutions for electrical impedance tomography based on conjugate gradients methods," *Measurement Science and Technology*, Vol. 13, 101–117, 2002.
10. Borsic, A., et al., "In vivo impedance imaging with total variation regularization," *IEEE Transactions on Medical Imaging*, Vol. 29, No. 1, 44–53, 2010.
11. Lukaschewitsch, M., P. Maass, and M. Pidcock, "Tikhonov regularization for electrical impedance tomography on unbounded domains," *Inverse Problems*, Vol. 19, 585–610, 2003.
12. Fan, W., H. Wang, et al., "An image reconstruction algorithm based on preconditioned LSQR for 3D EIT," *IEEE International Instrumentation and Measurement Technology Conference*, 10, 2011.
13. Jacobsen, M., P. C. Hansen, and M. A. Saunders, "Subspace preconditioned LSQR for discrete ill-posed problems," *BIT Numerical Mathematics*, Vol. 43, 975–989, 2003.
14. Wang, H. X., L. Tang, and Y. Yan, "Total variation regularization algorithm for electrical capacitance tomography," *Chinese Journal of Scientific Instrument*, Vol. 28, No. 11, 2014–2018, 2007.
15. Chambelle, A., et al., "An algorithm for total variation minimization and applications," *Journal of Mathematical Imaging and Vision*, Vol. 20, 89–97, 2004.
16. Yang, Y., H. Wu, et al., "Image reconstruction for electrical impedance tomography using enhanced adaptive group sparsity with total variation," *IEEE Sensors Journal*, Vol. 17, No. 17, 5589–5598, 2017.
17. Hemming, B., A. Fagerlund, and A. Lassila, "Linearized solution to electrical impedance tomography based on the schur conjugate gradient method," *Measurement Science & Technology*, Vol. 18, No. 11, 3373, 2007.
18. Li, X., X. Chen et al., "Electrical-impedance-tomography imaging based on a new three-dimensional thorax model for assessing the extent of lung injury," *AIP Advances*, Vol. 10, 9000000, 2019.

19. Kolda, T. and B. Bader, "Tensor decompositions and applications," *SIAM Rev.*, Vol. 51, No. 3, 455–500, 2009.
20. De Lathauwer, L., B. De Moor, and J. Vandewalle, "A multilinear singular value decomposition," *SIAM J. Matrix Anal. Appl.*, Vol. 21, 1253–1278, 2000.
21. Wang, Q., P. Zhang, et al., "Patch-based sparse reconstruction for electrical impedance tomography," *Sensor Review*, Vol. 37, No. 3, 257–269, 2017.
22. Caiafa, C. F. and A. Cichocki, "Fast and stable recovery of approximately low multilinear rank tensors from multi-way compressive measurements," *IEEE Int. Conf. Acoust. Speech, Signal.*, 6790–6794, 2014.
23. Caiafa, C. F. and A. Cichocki, "Multidimensional compressed sensing and their applications," *Wiley Interdisciplinary Rev.: Data Mining Knowledge Discovery*, Vol. 3, No. 6, 355–380, 2013.
24. Hansen, P. C., "Rank-deficient and discrete Ill-posed problems," *American Mathematical Monthly*, Vol. 10, No. 3, 215–247, 1998.
25. Caiafa, C. F. and A. Cichocki, "Stable, robust, and super fast reconstruction of tensors using multi-way projections," *IEEE Transactions on Signal Processing*, Vol. 63, No. 3, 780–793, 2015.
26. Schullcke, B., Z. S. Krueger, and B. Gong, "Ventilation inhomogeneity in obstructive lung diseases measured by electrical impedance tomography: A simulation study," *J. Clin. Monit. Comput.*, Vol. 32, No. 4, 753–761, 2018.
27. Schullcke, B., Z. S. Krueger, and B. Gong, "A simulation study on the ventilation inhomogeneity measured with electrical impedance tomography," *IFAC Papers on Line*, Vol. 50, 8781–8785, 2017.
28. Wang, Q., H. X. Wang, et al., "Image reconstruction based on L1 regularization and projection methods for electrical impedance tomography," *Review of Scientific Instruments*, Vol. 83, No. 10, 104707, 2012.